



Photocatalytic degradation of Orange G using TiO₂/Fe₃O₄ nanocomposites

B. Mercyrani¹ · R. Hernandez-Maya² · M. Solís-López¹ · Christeena Th-Th¹ · S. Velumani^{1,2}

Received: 1 December 2017 / Accepted: 6 April 2018 / Published online: 18 April 2018
© Springer Science+Business Media, LLC, part of Springer Nature 2018

Abstract

Titanium dioxide (TiO₂) is one among the best photocatalysts used in commercial applications. However, its large intrinsic bandgap (~ 3.23 eV) limits its photocatalytic application only to the ultraviolet (UV) region that is only 4% of the solar spectrum. The recombination of photogenerated electron–hole pairs reduces the quantum efficiency and photocatalytic activity. The visible region allows us to use 43% of the solar spectrum. Therefore, to extend the photocatalytic activity of TiO₂ to visible light spectrum, its bandgap must be decreased that suppresses the recombination reactions. This can be achieved by coupling of semiconductor metal oxides having different bandgap values with TiO₂ for the efficient use in the visible light region. In this work, magnetite (Fe₃O₄) nanoparticles were synthesized by a modified co-precipitation method, and it was used to prepare a TiO₂/Fe₃O₄ nanocomposite with three different ratios (0.2/0.8, 0.5/0.5, and 0.8/0.2). The obtained nanocomposite was characterized using X-ray diffraction, Raman and ultraviolet–visible spectroscopies, and scanning electron microscopy fitted with scanning transmission electron microscopy to understand the various properties such as crystallinity, optical properties, and morphology of the nanocomposites. We noticed that the crystallite size of TiO₂ in the nanocomposite, as well as the bandgap energy of the nanocomposite, decreases with the increasing Fe₃O₄ content. The degradation of Orange G with Fe₃O₄, TiO₂, and nanocomposites with three different ratios was studied in a solar simulator under different exposure times. Our studies show that (TiO₂)_{0.2}(Fe₃O₄)_{0.8} nanocomposite having small crystallite size and bandgap gives the best photocatalytic activity under visible light among other ratios.

1 Introduction

Water is regarded as one of the essential needs of the human-kind [1]. Although it is an abundant resource on mother Earth, as per various organizations like world health organization (WHO), the availability of safe drinking water for human consumption around the world is less than 1% [2]. The ever-growing population and the technological needs amidst the environmental issues challenge the supply of potable water without various organic and inorganic

pollutants [3]. The presence of non-biodegradable effluents such as heavy metal ions (arsenic, zinc, copper, nickel, mercury, cadmium, lead, and chromium) are not only classified as carcinogens but are also harmful to the environment [4, 5]. Also, various industrial pollutants (e.g., organic dyes) such as methylene blue (MB), Rhodamine B (RhB), Rhodamine 6G (Rh6G), methyl orange (MO), and organic chemicals like phenol and toluene poses a severe threat to the global ecosystem that needs to be addressed [6]. Traditional large-scale water treatment systems such as coagulation, sedimentation, filtration, chemical and membrane technologies are not only expensive but also produce toxic pollutant byproducts [7, 8]. Nevertheless, such techniques are not efficient enough to completely remove the contaminants to meet the water quality standards [9, 10]. Therefore, the urge for a well-defined technology is required to cope with the global scarcity of potable water.

Nanotechnology has the potential to resolve the current issue of water crisis [11]. The technology for water purification must have the ability of efficiently removing the toxic contaminants by a rapid and safe route within the

✉ S. Velumani
velu@cinvestav.mx

¹ Programa de Nanociencias y Nanotecnología, Centro de Investigación y de Estudios Avanzados del Instituto Politécnico Nacional (CINVESTAV-IPN), Mexico City, Mexico

² Departamento de Ingeniería Eléctrica (SEES), Centro de Investigación y de Estudios Avanzados del Instituto Politécnico Nacional (CINVESTAV-IPN), Av. Instituto Politécnico Nacional 2508, Col. San Pedro Zacatenco, Mexico City 07360, Mexico

cost-framework. The main advantages of using nanomaterials are the large surface area and high reactivity that can play a significant role in water purification increasing the water quality [12]. The “Advanced Oxidation Processes (AOPs)” is an innovative field for the water treatment where the mechanism is the in-situ generation of highly reactive transitory species (i.e., H_2O_2 , $\text{OH}\cdot$, $\text{O}_2^{\cdot-}$, O_3) that mineralize refractory organic compounds, water pathogens, and disinfection byproducts [13]. Heterogeneous photocatalysis, which is one among AOPs, employs semiconductor catalysts like ZnS, ZnO, Fe_3O_4 , CdS, GaP, TiO_2 and BiVO_4 [14–16]. These semiconductor catalysts have its efficiency for degrading a wide range of hazardous refractory organics into nontoxic, biodegradable compounds, and finally mineralized into carbon dioxide and water [17].

Among various semiconductor catalysts, Titania (TiO_2) has gained much attention in photocatalysis technology. It is the most active photocatalysts with a photon energy between 300 and 390 nm remaining stable even after the repeated catalytic cycle [18]. TiO_2 catalyst has got chemical and thermal stability that is crucial for the photocatalytic treatment. TiO_2 exists in three polymorphs, anatase ($E_g = 3.2$ eV), rutile ($E_g = 2.96$ eV), and brookite ($E_g = 2.96$ eV), and among the three phases, anatase type TiO_2 is considered as the most stable phase for photocatalysis [19, 20]. The high photocatalytic activity of TiO_2 is due to its surface area, size, pore volume, pore structure and crystalline phases [21]. The bandgap of TiO_2 varies from 3 to 3.2 eV that destroys most of the chemical bonds such as C–C, C–H, C–N, C–O, and N–H [22, 23]. Although TiO_2 itself is the best photocatalyst, its large intrinsic bandgap energy (~3.23 eV), severely limits its photocatalytic application [24–31]. The recombination of photogenerated electron–hole pairs reduces the quantum efficiency and photocatalytic activity [32]. Moreover, it is difficult to retrieve the water dispersed TiO_2 . Therefore, a better approach is to be adopted to resolve this critical issue without compromising the photocatalytic activity. Magnetic nanomaterials that are also photocatalysts comes handy in such circumstances where it is necessary to not only enhance the photocatalytic active but also possible to retrieve the photocatalysts as well.

Magnetic iron oxide nanoparticles have better optical, chemical, magnetic, electrical and thermal properties that enabled it to be used in various applications such as in consumer electronics, catalysis, ferrofluids, data storage, and biomedical as well as in pigments [33, 34]. Iron oxide exists in various forms like hematite ($\alpha\text{-Fe}_2\text{O}_3$), maghemite ($\gamma\text{-Fe}_2\text{O}_3$), and magnetite (Fe_3O_4) where maghemite and magnetite are widely used in photocatalysis [35–37]. However, the large surface to volume ratio of iron oxide nanoparticles results in high surface energies and tend to aggregate [38]. Iron oxide nanoparticles are readily oxidized in the air due to their high reactivity that decreases

their dispensability and magnetic behavior. Therefore, it is essential to maintain the stability of the iron oxide that can be achieved by efficient passivation of the nanoparticles with organic ligands, polymers, and monomers [39–41]. Aggregation of Fe_3O_4 nanoparticles results in the reduction of surface-active regions that are required for an improved light scattering. Therefore, the pristine magnetite nanoparticles have to be modified with TiO_2 for the highest photocatalytic degradation. A high surface area can result in more affinity to hydroxyl groups present in the material and hence produce hydroxyl radicals. The produced hydroxyl radicals are the major oxidants needed for degrading organic compounds like various dyes. When magnetite modifies TiO_2 nanoparticles, it will give rise to small particle size and low bandgap nanocomposites. Another fact is that the higher recombination rate of magnetite nanoparticles is due to the low bandgap. The presence of titania coating over magnetic nanoparticles acts as a charge scavenger that in turn reduce the recombination rate, and thus increases the photocatalytic activity [42]. Experiments on photocatalysis are mostly done with the help of synthetic dyes because of its ease of visualization and interpretation. Synthetic dyes are those molecules that are poly-aromatic that give permanent color to materials like textile fabrics. The applications of the synthetic dyes will go with textile, paper, food, cosmetics, and pharmaceutical industries. Among all, the textile industry is the most extensive consumer, and thus, the most substantial polluter. Azo dyes, which are grouped under synthetic dyes possess one or more $-\text{N}=\text{N}-$ groups, are considered as the significant group that is widely used in the textile industry constitutes 60–70% due to low-cost and straightforward synthetic route. Also, they are stable and can contribute a variety of colors. They are electron deficient xenobiotic compounds as they have electron withdrawing groups that generates electron deficiency in the molecule resulting in degradation resistant. Also, the low binding and inefficiency during dyeing that releases 10–50% of unused dye directly into the water [43]. Here for our study, Orange G was selected as the model dye, which is also an azo dye.

In this work, we have discussed the synthesis of magnetite using co-precipitation method and $(\text{TiO}_2)_x(\text{Fe}_3\text{O}_4)_{1-x}$ ($x = 0.2, 0.5, \text{ and } 0.8$) nanocomposites by a modified low-temperature method. When TiO_2 is annealed at high temperature, Fe_3O_4 phase changes to antiferromagnetic $\alpha\text{-Fe}_2\text{O}_3$ phase. Therefore, a low-temperature method was followed to maintain Fe_3O_4 and TiO_2 phases which are easy to synthesize and yields good results, and there is no phase change of Fe_3O_4 . There was a superior photocatalytic activity under visible light by modified magnetic nanoparticles with titanium dioxide. The used materials can be easily retrieved and reused after the photocatalytic activity due to its strong magnetic properties [44, 45]. We have, to the best of our knowledge, also reporting, for the first time, the photocatalytic

degradation of the Orange G using thus synthesized nanocomposites. The nanocomposites exhibited a superior photocatalytic activity under visible light, and the results are thus discussed in detail.

2 Experimental

2.1 Materials

All the chemicals used in this work are of analytical grade and was used without any further purification. Iron(III) chloride hexahydrate ($\text{FeCl}_3 \cdot 6\text{H}_2\text{O}$), Iron(II) chloride tetrahydrate ($\text{FeCl}_2 \cdot 4\text{H}_2\text{O}$), ammonium hydroxide (NH_4OH), titanium(IV) oxide (anatase), and ethanol ($\text{C}_2\text{H}_6\text{O}$) were purchased from Sigma Aldrich. Nitrogen gas cylinder was bought from INFRA, Mexico.

2.2 Synthesis of magnetite using co-precipitation method

Among various methods for the synthesis of magnetite nanoparticles, the co-precipitation method is considered as the best due to its simplicity and high productivity, shown in Fig. 1. The ferric chloride (Fe^{2+}) and ferrous chloride

(Fe^{3+}) are mixed in 2:1 ratio in 100 mL of deionized water at room temperature. Ammonium hydroxide solution was added, dropwise, to that mixture under continuous stirring and constant flow of nitrogen, until the formation of black precipitates. The black precipitate is then recovered and washed several times with deionized water. The final precipitate along with the suspended particles was collected with the help of a strong magnet, and the material was dried in an oven at 70°C for overnight. Thus, obtained black crystals were powdered using a pestle and mortar [46].

2.3 Synthesis of $\text{TiO}_2/\text{Fe}_3\text{O}_4$ nanocomposite

$(\text{TiO}_2)_x(\text{Fe}_3\text{O}_4)_{1-x}$ ($x = 0.2, 0.5, \text{ and } 0.8$) were prepared by the following method shown in Fig. 2. Solution A consists of TiO_2 in 20 mL of ethanol. Solution B consists of Fe_3O_4 in 5 mL of deionized water. Both solutions were individually ultrasonicated for 30 min to get a uniform dispersion of the solutes. Subsequently, solution B (magnetite) was added slowly, in a dropwise manner, to solution A (TiO_2) under ultrasonication until the formation of a uniform dispersion. The final precipitate was washed several times with deionized water and dried an oven at 70°C for overnight to get $\text{TiO}_2/\text{Fe}_3\text{O}_4$ nanocomposite powder.

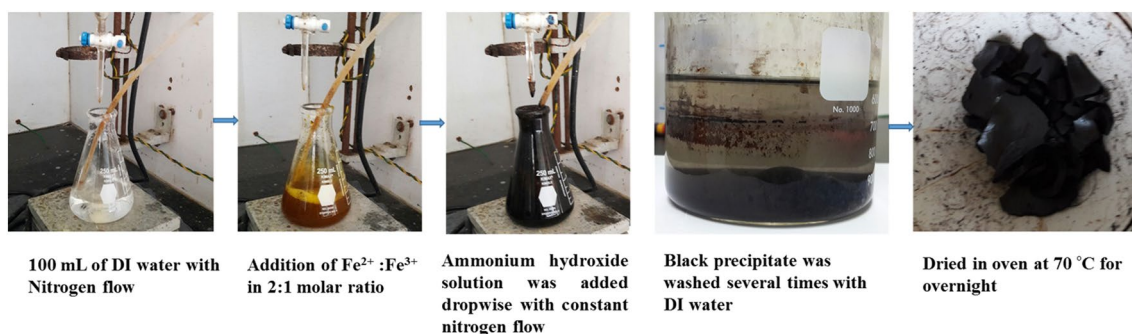


Fig. 1 Synthesis of magnetite using co-precipitation method

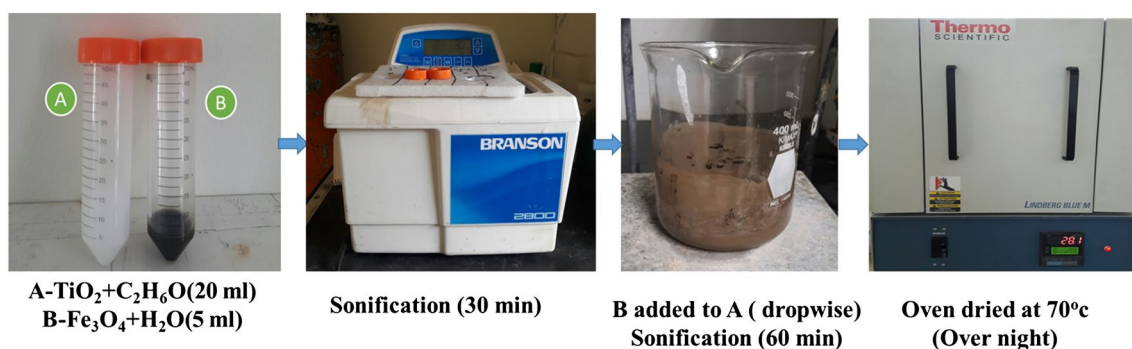


Fig. 2 Synthesis of the nanocomposite material of $(\text{TiO}_2)_x(\text{Fe}_3\text{O}_4)_{1-x}$ ($x = 0.2, 0.5, \text{ and } 0.8$)

2.4 Characterization

The crystallinity and phase analyses were assessed using a Bruker D2 Phaser XRD equipment, in the 2θ range from 20° to 80° with a step size of 0.02° . Elemental composition and morphological analyses were performed on Tescan-Vega 3 SEM, at an accelerating voltage of 10 KV, equipped with STEM and Bruker EDX detectors. A dispersion of the nanocomposite material was prepared in a solution of sodium dodecyl sulfate in deionized water, and a drop was deposited on an amorphous carbon-coated copper grid, and the dried sample was analyzed with the STEM at an accelerating voltage of 30 KV. The bandgap energy was determined using UV–Visible diffuse reflectance spectrophotometric (UV–Vis DRS) analysis on powders (Agilent-carry-5000 spectrophotometer). Raman scattering spectra were recorded, between 100 and 1000 cm^{-1} at ambient temperature, on Horiba-Jobin-Yvon spectrometer (Lab RAM HR800) with a helium–neon laser ($\lambda = 632.8\text{ nm}$) as the excitation source. The photocatalytic activity was performed using reflective solar simulator equipped with a 1.6 kW ozone-free xenon arc lamp (SCIENCETECH VHE-NL-200) at an intensity of 500 W m^{-2} at ambient temperature (approx. $23 \pm 2^\circ\text{C}$), and the corresponding absorbance measurement was recorded, between 200 and 800 nm, on the Jasco V-60 UV–visible spectrophotometer.

2.5 Photocatalytic activity

The photocatalytic activity was carried out by the reaction suspensions containing Orange G in an aqueous solution (50 mg/L, 50 mL) with the catalyst of TiO_2 , Fe_3O_4 , and $(\text{TiO}_2)_x(\text{Fe}_3\text{O}_4)_{1-x}$ ($x = 0.2, 0.5, \text{ and } 0.8$) of (1 g/L). The catalyst was added to the Orange G solution and mechanically stirred in the darkroom for 20 min to ensure adsorption/desorption equilibrium. Subsequently, the reaction suspension was irradiated by visible light using solar simulator at various periods (0–120 min). The concentration of Orange G was determined by measuring the value at 476 nm obtained from the calibration curve [31]. After the experiment, the powders were collected with the help of the strong magnet and washed several times with deionized water and dried in an oven at 70°C for the further use.

3 Results and discussions

3.1 XRD analysis

To understand the crystallinity and phase formation of the synthesized materials, we assessed the powder samples by XRD. The diffraction pattern of the synthesized magnetite, as shown in Fig. 3a, showed peaks at 30.14° , 35.50° , 43.15° ,

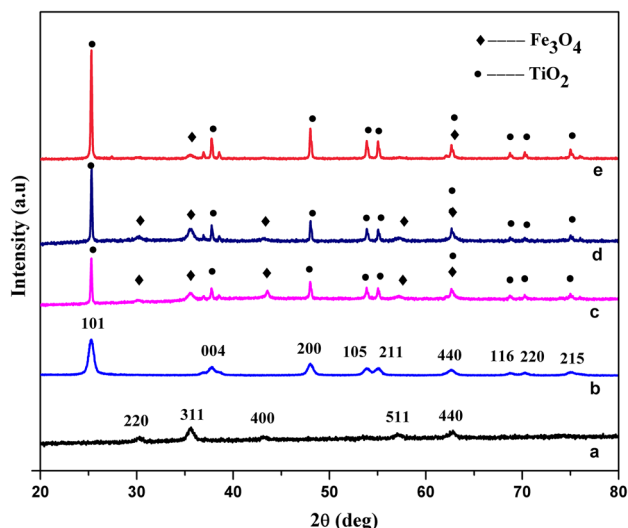


Fig. 3 X-ray diffractograms of the synthesized materials: (a) Fe_3O_4 , (b) TiO_2 , (c) T/M-0.2/0.8, (d) T/M-0.5/0.5, and (e) T/M-0.8/0.2

57.07° , and 62.67° identified with the planes (220), (311), (400), (511), and (440), respectively, of the typical inverse cubic spinel structure of Fe_3O_4 (ICDD card no. 71-6336). Figure 3b shows the diffraction pattern for TiO_2 , where the position of the diffraction peaks at 25.28° , 37.80° , 48.04° , 53.88° , 55.06° , 62.68° , 68.76° , 70.30° , and 75.02° corresponding to planes (101), (004), (200), (105), (211), (204), (116), (220), and (215), respectively, to the tetragonal structure of TiO_2 (anatase-ICDD card no. 21-1272). The results are well matched with the previous reports [47, 48].

The sharp and intense peaks represent the crystallinity of TiO_2 and Fe_3O_4 . Figure 3 c, d, e represent the nanocomposite of $\text{TiO}_2/\text{Fe}_3\text{O}_4$ with three different proportions 0.2/0.8, 0.5/0.5, and 0.8/0.2, respectively. The $(\text{TiO}_2)_{0.2}(\text{Fe}_3\text{O}_4)_{0.8}$ nanocomposite shows all the peaks of TiO_2 and Fe_3O_4 . However, with the increase of TiO_2 content, the photocatalytic activity of the nanocomposite decreases.

The coherently diffracting domain (or crystallite) size of the TiO_2 in the nanocomposite was estimated, in the [101] crystallographic direction, using the Scherrer equation (Eq. 1) [49].

$$D = \frac{k\lambda}{\beta \cos \theta} \quad (1)$$

where K —the Scherrer constant (0.94, assuming spherical crystallites), λ —the wavelength of $\text{Cu-K}\alpha_1$ (1.5405 \AA), β —full width at half maximum (FWHM) value, θ —the Bragg's angle (radians).

Therefore, the crystallite size of the TiO_2 in the nanocomposites, for the weight ratios 0.8/0.2, 0.5/0.5, and 0.2/0.8, is estimated as 36.73, 31.82, and 29.50 nm, respectively. It is apparent that the crystallite size of TiO_2 decreases with the increase in Fe_3O_4 content as shown in Table 1.

Table 1 The crystallite size and band gap of Fe_3O_4 , TiO_2 , and $(\text{TiO}_2)_x(\text{Fe}_3\text{O}_4)_{1-x}$ ($x = 0.2, 0.5, \text{ and } 0.8$) (T/M) nanocomposites

Materials	Crystallite size (nm)	Bandgap (eV)
TiO_2 (T)	17.62	3.2
Fe_3O_4 (M)	13	1.98
T/M 0.8/0.2	36.73	3.35
T/M 0.5/0.5	31.82	$E_{g1} = 2.70$ $E_{g2} = 2.85$
T/M 0.2/0.8	29.50	$E_{g1} = 2.35$ $E_{g2} = 2.65$

3.2 SEM analysis

The scanning electron micrographs of the nanocomposites are shown in Fig. 4. The micrographs showed the broad distribution of the nanoparticles forming several clusters. The $(\text{TiO}_2)_{0.5}(\text{Fe}_3\text{O}_4)_{0.5}$ nanocomposite showed a more homogeneous distribution [50]. For comparison, we have also studied the synthesized magnetite crystals that were crushed using a pestle and mortar.

The SEM shows large pieces, chunks of several μm in dimensions along with finer particles, and agglomerates of various sizes. Some of these chunks also been noticed in the SEM images of the nanocomposite. As drying process promotes agglomeration/aggregation of nanoparticles, especially with the magnetite nanoparticles due to dipole interactions, it is not uncommon to notice such chunks [42].

3.3 STEM analysis

To determine and distinguish the distribution of nanoparticle in the synthesized nanocomposites, we have carried out the STEM analysis on the best photocatalytic component

$(\text{TiO}_2)_{0.2}(\text{Fe}_3\text{O}_4)_{0.8}$ nanocomposites in bright and dark field imaging mode. As we can observe in the dark field image of Fig. 5, the denser Fe_3O_4 particles, appearing darker, are surrounded by lighter TiO_2 nanoparticles [51]. The magnetite particles are of diverse sizes ranging from few hundred nanometers to several micrometers were seen neighbored by nanoparticles of TiO_2 . Finer nanocomposites that are specially composed of TiO_2 nanoparticles are significant for the higher photocatalytic activity, and the STEM analysis confirms the composites of the synthesized materials. The image analysis was performed using Gatan Inc., Digital Micrograph software.

3.4 Raman analysis

According to the factor group analysis, TiO_2 has six modes $A_{1g} + 2B_{1g} + 3E_g$ that are Raman active. Totally 15 normal modes of vibration are there for TiO_2 . The Raman spectra of Fe_3O_4 , TiO_2 , and nanocomposites are shown in Fig. 6. For the Raman spectrum of anatase, the frequencies of the Raman band are observed at 152, 206, 405, 523, and 647 cm^{-1} . The 152 cm^{-1} band is the strongest among all observed bands of anatase. The three bands at 152, 206, and 647 cm^{-1} are assigned to the E_g modes, and the band at 405 cm^{-1} to the B_{1g} mode whereas the band 523 cm^{-1} is the doublet of the A_{1g} and B_{1g} modes [52]. Magnetite structure exhibits 14 Raman active modes ($3A_1 + 3E + 8T_2$) and is detected by the occurrence of the splitting of E_g and T_{2g} modes. Here in this spectrum, 226 is assigned to the T_{2g} mode, and 306 is assigned to the E_g mode [53]. For magnetite, only two modes could be seen, due to weak Raman scattering [54].

Fig. 4 SEM images of **a** crushed synthesized magnetite (Fe_3O_4) crystals, **b** $(\text{TiO}_2)_{0.2}(\text{Fe}_3\text{O}_4)_{0.8}$ nanocomposites at 5 kx magnification, **c** $(\text{TiO}_2)_{0.2}(\text{Fe}_3\text{O}_4)_{0.8}$ nanocomposites at $\times 20\text{k}$ magnification, **d** $(\text{TiO}_2)_{0.5}(\text{Fe}_3\text{O}_4)_{0.5}$, and **e** $(\text{TiO}_2)_{0.8}(\text{Fe}_3\text{O}_4)_{0.2}$ at $\times 5\text{k}$ magnification

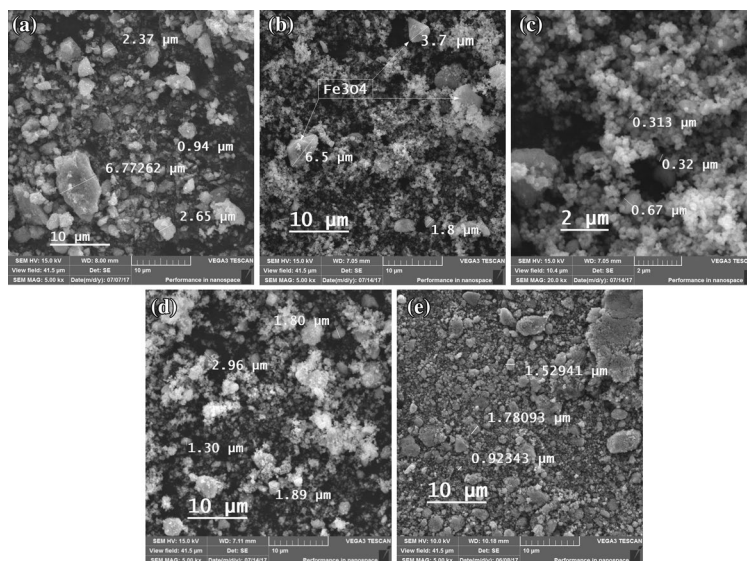


Fig. 5 Image obtained by STEM of the nanocomposite material of $(\text{TiO}_2)_x(\text{Fe}_3\text{O}_4)_{1-x}$ ($x=0.2$)

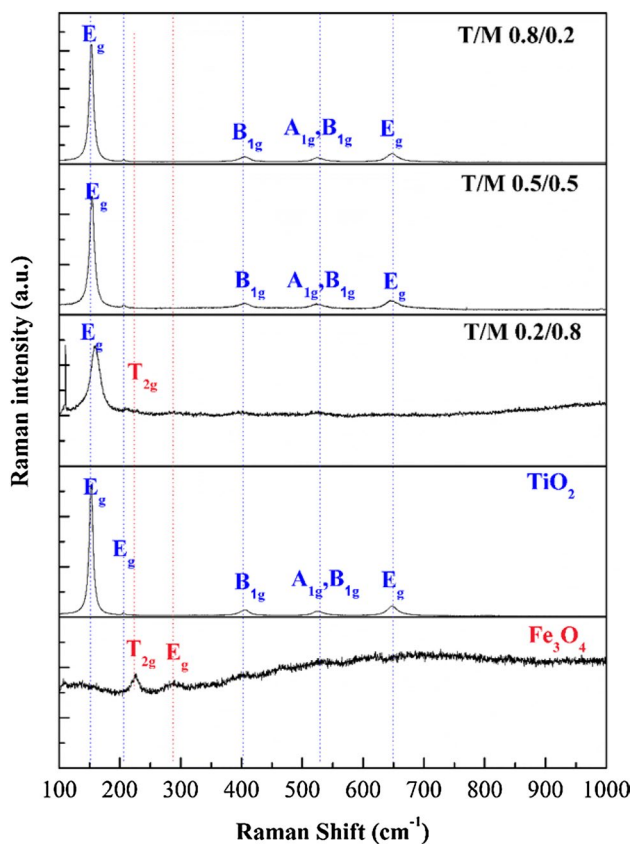
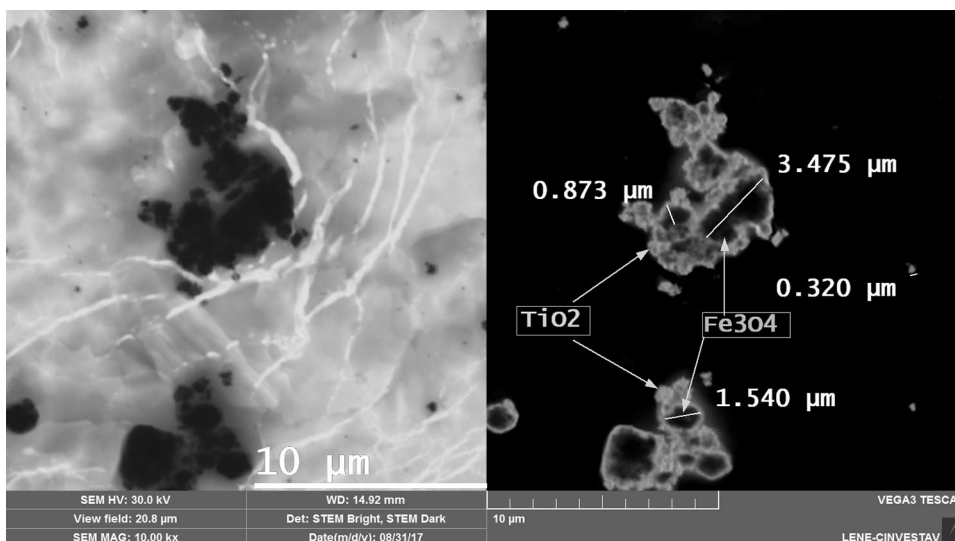


Fig. 6 Raman analysis of Fe_3O_4 , TiO_2 , and $(\text{TiO}_2)_x(\text{Fe}_3\text{O}_4)_{1-x}$ ($x=0.2, 0.5, \text{ and } 0.8$) (T/M) nanocomposites

3.5 UV-Visible diffuse reflectance spectrophotometric analysis

The photocatalytic property of the synthesized nanocomposites was studied with the help of UV-Vis DRS. By the

calculated bandgap values, we can understand the structural variation of the synthesized materials. The generalized equation to calculate the bandgap of the materials using Kubelka–Munk function is given in Eq. 2,

$$F(R) = (1 - R)^2 / 2R \tag{2}$$

where R is the reflectance, F(R) is proportional to the extinction coefficient (α).

This equation is applicable to highly light scattering materials and absorbing particles. The bandgap of the materials is obtained by plotting modified Kubelka–Munk function, $(F(R) \cdot h\nu)^n$, vs. $h\nu$ and extrapolating the linear part of the graphics to the abscissa, where, $n=1/2$ for the direct transition, and $n=2$ for an indirect transition [55]. The $h\nu$ is the energy in terms of eV and is obtained from Eq. 3,

$$E_g = h\nu = \frac{hc}{\lambda} = \frac{1243}{\lambda} \tag{3}$$

where h and c are constants, and λ is the wavelength observed.

The bandgap value of TiO_2 (anatase phase) is 3.2 eV [56] and for magnetite, it varies from 0 to 3 eV [22]. For the synthesized nanocomposite materials, the bandgaps are obtained by plotting $(F(R) \cdot h\nu)^2$ vs. $h\nu$ as shown in Fig. 7, considering an indirect transition of the materials. The extrapolation of the $(\text{TiO}_2)_{0.8}/(\text{Fe}_3\text{O}_4)_{0.2}$ nanocomposite gives the bandgap of 3.35 eV. While, the other two nanocomposite ratios each resulted in exhibiting two different bandgaps, which could be attributed to the spin-orbit splitting of the valence band [57], listed as E_{g1} and E_{g2} for lower and higher energies, respectively. The bandgaps of the synthesized nanocomposite materials along with the precursors are listed in Table 1. The addition of Fe_3O_4 promotes the transfer of electrons from valence band to the conduction band resulting in the decrease of the bandgap of TiO_2 in the nanocomposite [31].

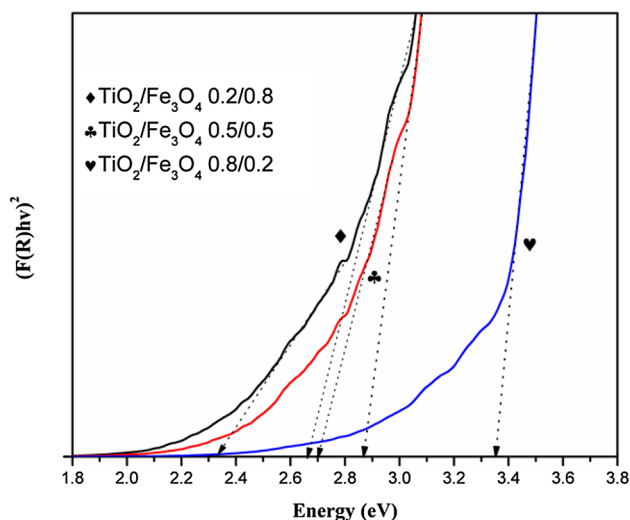


Fig. 7 Diffuse reflectance spectra of $(\text{TiO}_2)_x(\text{Fe}_3\text{O}_4)_{1-x}$ ($x=0.2, 0.5$, and 0.8) nanocomposites

3.6 Photocatalytic activity measurements using Orange G

Figure 8 shows the photocatalytic degradation of Orange G using TiO_2 , Fe_3O_4 and $(\text{TiO}_2)_x(\text{Fe}_3\text{O}_4)_{1-x}$ ($x=0.2, 0.5$, and 0.8).

The percentage of degradation of each material is calculated by the formula (Eq. 4) [41].

$$\text{Degradation \%} = \frac{C_0 - C}{C_0} \times 100 \quad (4)$$

where C_0 is the initial concentration of the dye, C is the concentration of the dye at different times, t .

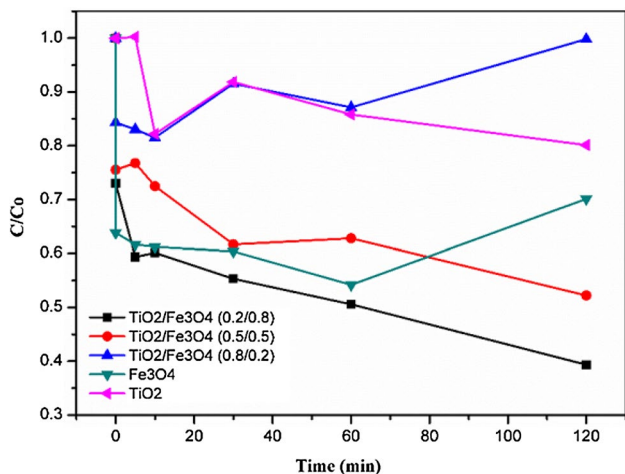


Fig. 8 Photocatalytic degradation of Orange G using TiO_2 , Fe_3O_4 , and for the three $\text{TiO}_2/\text{Fe}_3\text{O}_4$ nanocomposite ratios

By the XRD and UV results, by increasing the amount of Fe_3O_4 , the crystallite size and the bandgap of TiO_2 in the nanocomposite decreases, leading to the increase in the photodegradation of Orange G, however, with the increase of TiO_2 content, the photocatalytic activity of the nanocomposite decreases as shown in Fig. 8. The lowest bandgap of the magnetite results in high recombination rate. Magnetite alone shows the photocatalytic activity in the visible region, but the aggregation of magnetite nanoparticles reduces the surface-active regions and prevents the light to pass through the material [42]. The TiO_2 reduce the recombination rate and enhances the photocatalytic activity of magnetite. The degradation percentage of each material is shown in Fig. 9. From the graph, it is clear that $(\text{TiO}_2)_{0.2}(\text{Fe}_3\text{O}_4)_{0.8}$ nanocomposite shows the best photocatalytic property among all other materials.

3.7 Photocatalytic mechanism

The mechanism of semiconductor photocatalysis involves the use of photon energy which is equal to or beyond the band gap of the semiconductor photocatalyst used. The electrons will be excited from the valence band (VB) to the conduction band (CB) leaving behind an electron vacancy or a hole in the valence band (Eqs. 5, 6) [58]. As a result, a reduction reaction between the electrons took place in the conduction band and electron acceptors, such as adsorbed O_2 molecules, which produce superoxide radical anions (Eq. 7) [59]. The formed holes can either oxidize organic compound directly or trap by electron donors, and H_2O_2 is formed due to recombination of these oxidant radicals (Eqs. 8, 9). This H_2O_2 can react with the superoxide radical anion thus regenerating hydroxyl radical (Eq. 10). Both superoxide anion and

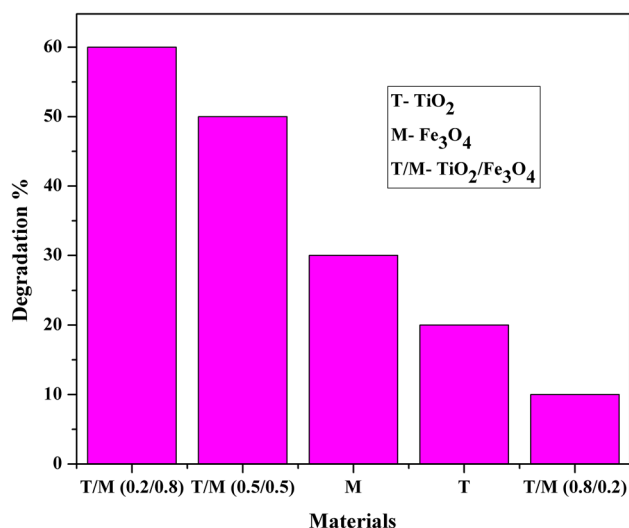
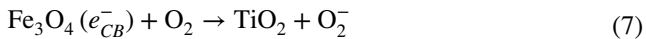
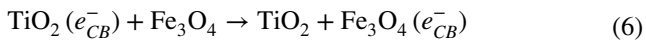
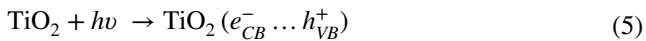


Fig. 9 Degradation percentage of Orange G using TiO_2 , Fe_3O_4 and for the three $\text{TiO}_2/\text{Fe}_3\text{O}_4$ nanocomposite ratios

hydroxyl radicals help in the decomposition of the Orange G dye to non-toxic by-products (CO_2 , H_2O , and mineral acids) on exposure to sunlight irradiation (Eqs. 11, 12) [60]. Magnetite has an excellent light absorption capability as well as the ability to modify the bandgap of any material in the nanocomposite thereby enabling its activity in the visible spectra [38].

The degradation mechanisms involve:



4 Conclusion

In this work, the Fe_3O_4 nanoparticles were synthesized by the co-precipitation method, and with the help of this, the $(\text{TiO}_2)_x(\text{Fe}_3\text{O}_4)_{1-x}$ ($x = 0.2, 0.5$, and 0.8) nanocomposites were synthesized. SEM analysis reveals the aggregation of magnetite particles. However, the addition of TiO_2 decreases the aggregation of magnetite. Nevertheless, it was inferred that the increasing amount of the magnetite decreases both the crystallite size and the bandgap of the TiO_2 in the nanocomposite. The lower bandgap and smaller crystallite size of the TiO_2 in the $(\text{TiO}_2)_{0.2}(\text{Fe}_3\text{O}_4)_{0.8}$ nanocomposite resulted in the best photocatalytic activity (60%) among other samples in degradation of Orange G.

Acknowledgements The authors are thankful to Consejo Nacional de Ciencia y Tecnología (The National Council of Science and Technology-CONACYT-Mexico) for providing the financial support from the project CONACYT-SENER 263043. B. Mercyrani wishes to thank CONACYT for the doctoral fellowship and to Srikanth Chakaravarthy for his valuable suggestions and corrections. Authors also wish to thank F. Alvarado-Cesar (XRD & SEM), Miguel Galvan Arellano (Raman analysis) and J.C. Duran-Alvarez (UV-Vis DRS analysis).

References

1. R. Das, S.B. Abd Hamid, Md.E. Ali, A.F. Ismail, M.S.M. Annuar, S. Ramakrishna, *Desalination* **354**, 160–179 (2014)
2. A.S. Adeleye, J.R. Conway, K. Garner, Y. Huang, Y. Su, A.A. Keller, *Chem. Eng. J.* **286**, 640–662 (2016)

3. R.P. Schwarzenbach, B.I. Escher, K. Fenner, T.B. Hofstetter, C.A. Johnson, U. von Gunten, B. Wehrli, *Science* **313**, 1072–1077 (2016)
4. S.K. Kansal, M. Singh, D. Sud, J. Hazard. Mater. **141**, 581–590 (2007)
5. Y.F. Shen, J. Tang, Z.H. Nie, Y.D. Wang, Y. Ren, L. Zuo, *Sep. Purif. Technol.* **68**, 312–329 (2009)
6. A. Reife, H.S. Fremann, *Environmental chemistry of dyes and pigments* (Wiley, New York, 1996), pp 753–784
7. P.V.A. Padmanabhan, K.P. Sreekumar, T.K. Thiyagarajan, R.U. Satpute, K. Bhanumurthy, P. Sengupta, G.K. Dey, K.G.K. Warrior, *Vacuum* **80**, 11–12 (2006)
8. U.I. Gaya, A.H. Abdullah, *J. Photochem. Photobiol. C* **9**, 1–12 (2008)
9. N. Ferroudj, J. Nzimoto, A. Davidson, D. Talbot, E. Briot, V. Dupuis, A. Bée, *App. Catal. B* **136**, 9–18 (2013)
10. L. Qiu, Y. Peng, B. Liu, B. Lin, Y. Peng, M.J. Malik, F. Yan, *Appl. Catal. A* **413**, 230–237 (2012)
11. M. Tillie, M. Munasinghe, Y. Hlope, *Deraniyagala, Water Dev.* **2006**, 1–44 (2006)
12. S. Singh, K.C. Barick, D. Bahadur, *J. Hazard. Mater.* **192**, 1539–1547 (2011)
13. S. Esplugas, J. Gimenez, S. Conteras, E. Pascual, M. Rodriguez, *Water Res.* **36**, 1034–1042 (2002)
14. Y.M. Hunge, M.A. Mahadik, R.N. Bulakhe, S.P. Yadav, J.J. Shim, A.V. Moholkar, C.H. Bhosale, *J. Mater. Sci.: Mater. Electron.* **28**, 17976–17984 (2017)
15. R. Venkatesan, S. Velumani, K. Ordon, M. Makowska-Janusik, G. Corbel, A. Kassiba, *Mater. Chem. Phys* **205**, 325–333 (2018)
16. R. Venkatesan, S. Velumani, M. Tabellout, A. Kassiba, *J. Phys. Chem. Solids* **74**, 1695–1702 (2013)
17. M.N. Chong, B. Jin, W.K. Chow, C. Saint, *Water Res.* **44**, 2997–3027 (2010)
18. Y.-S. Li, J.S. Church, *J. Magn. Magn. Mater.* **324**(8), 1543–1550 (2012)
19. W. Wu, Q. He, C. Jiang, *Nanoscale Res. Lett.* **3**(11), 397–415 (2008)
20. A.K. Gupta, M. Gupta, *Biomaterials*, 26(18), 3995–4021 (2005)
21. M.A. López-Quintela, J. Rivas, *Curr. Opin. Colloid Interface Sci.* **1**(6), 806–819 (1996)
22. S. Shamaila, T. Bano, A.K.L. Sajjad, *Ceram Int* **43**, 14672–14677 (2017)
23. S. Malato, P. Fernandez-Ibanez, M.I. Maldonado, J. Blanco, W. Gernjak, *Catal. Today* **147**, 1–59 (2009)
24. J.C. Zhan, H. Zhang, G. Zhu, *Ceram. Int.* **40**, 8547–8559 (2014)
25. J. Chen, Y. Qian, X. Wei, *J. Mater. Sci.* **45**(22), 6018–6024 (2010)
26. Z. Liu, H. Bai, D.D. Sun, *New J. Chem.* **35**, 137–140 (2011)
27. L. Yuxiang, Z. Mei, G. Min, W. Xidong, *Rare Met.* **28**(5), 423 (2009)
28. C. Xu, A.S. Teja, *J. Supercrit. Fluids* **44**(1), 85–91 (2008)
29. C.Y. Wang, Z.Y. Chen, B. Cheng, Y.R. Zhu, H.J. Liu, *Mater. Sci. Eng. B* **60**(3), 223–226 (1999)
30. Y. Xu, S. Yang, G. Zhang, Y. Sun, D. Gao, Y. Sun, *Mater. Lett.* **65**(12), 1911–1914 (2011)
31. D. Beydoun, R. Amal, *J. Phys. Chem B* **104**, 4387–4396 (2000)
32. G. Marchegiani, P. Imperatori, A. Mari, L. Piloni, A. Chiolerio, P. Allia, P. Tiberto, L. Suber, *Ultrason. Sonochem.* **19**(4), 877–882 (2012)
33. K. Huang, Y. Lv, W. Zhang, S. Sun, *J. Mater. Res.* **18**, 939–945 (2015)
34. A.F. Shojaei, A.S. Nateri, *Superlattices Microstruct.* **88**, 211–224 (2015)
35. K.H. Choi, S.Y. Park, B.J. Park, J.S. Jung, *Surf. Coat. Technol.* **320**, 240–245 (2017)

36. X.L. Dong, X.Y. Mou, H.C. Ma, X.X. Zhang, X.F. Zhang, W.J. Sun, C. Ma, M. Xue, *J. Sol-Gel. Sci. Technol.* **66**(2), 231–237 (2013)
37. X. Yang, W. Chen, J. Huang, Y. Zhou, Y. Zhu, C. Li, *Sci. Rep.* (2015) <https://doi.org/10.1038/srep10632>
38. M.A. Zazouli, F. Ghanbari, M. Yousefid, S.M. Bidgol, *J. Environ. Chem. Eng.* **5**, 2459–2468 (2017)
39. Y. Zhu, L. Zhang, C. Gao, L. Cao, *J. Mater. Sci.* **35**, 4049–4054 (2000)
40. W. Zhanga, C. Hua, W. Zhaia, Z. Wanga, Y. Suna, F. Chia, S. Rana, X. Liua, Y. Lva, *Mater. Res.* **19**(3), 673–679 (2016)
41. A. Banisharif, S.H. Elahi, A.A. Firooz, A.A. Khodadadi, Y. Mortazavi, *Int. J. Nanosci. Nanotechnol.* **9**, 193–202 (2013)
42. H. Niu, Q. Wang, H. Liang, M. Chen, C. Mao, J. Song, S. Zhang, Y. Gao, C. Che, *Materials* **7**(5), 4034–4044 (2014)
43. R.P. Singh, P.K. Singh, R.L. Singh, *Toxicol. Int.* **21**(2), 160–166 (2014)
44. M. Morel, F. Martínez, E. Mosquera, *J. Magn. Magn. Mater.* **343**, 76–81 (2013)
45. R. Kumar, B.S. Inbaraj, B.H. Chen, *Mater. Res. Bull.* **45**(11), 1603–1607 (2010)
46. S.A. Kulkarni, *Int. J. Comput. Appl.* **66**(19), 20–24 (2012)
47. T. Xin, M. Ma, H. Zhang, J. Gu, S. Wang, M. Liu, Q. Zhang, *Appl. Surf. Sci.* **288**, 51–59 (2014)
48. M. Stefan, O. Pana, C. Leostean, C. Bele, D. Silipas, M. Senila, E. Gautron, *J. Appl. Phys.* **116** (2014). <https://doi.org/10.1063/1.4896070>
49. A. Bokare, H. Singh, M. Pai, R. Nair, S. Sabharwal, A.A. Athawale, *Mater. Res. Express* (2014). <https://doi.org/10.1088/2053-1591/1/4/046111>
50. W. Jiang, X. Zhang, X. Gong, F. Yan, Z. Zhang, *Int. J. Smart Nano. Mater.* **1**(4), 278–287 (2010)
51. P. Ma, W. Jiang, F. Wang, F. Li, P. Shen, M. Chen, Y. Wang, J. Liu, P. Li, *J. Alloys Compd.* **578**, 501–506 (2013)
52. A.G. Ilie, M. Scarisoareanu, I. Morjan, E. Dutu, M. Badiceanu, I. Mihailescu, *Appl. Surf. Sci.* **417**, 93–103 (2017)
53. P. Russo, D. Acierno, M. Palomba, G. Carotenuto, R. Rosa, A. Rizzuti, C. Leonelli, *J. Nanosci.* (2012). <https://doi.org/10.1155/2012/728326>
54. P.C. Panta, C.P. Bergmann, *J. Material Sci. Eng.* **5**, 1 (2015)
55. R. Lopez, R. Gomez, *J. Sol. Gel Sci. Technol.* **61**, 1–7 (2012)
56. S. Valencia, J.M. Marin, G. Restrepo, *Open Mater. Sci. J.* **4**, 9–14 (2010)
57. S. Velumani, X. Mathew, P.J. Sebastin, S.K. Narayanadas, D. Mangalraj, *Sol. Energy Mater. Sol. Cells* **76**, 347–358 (2003)
58. Z.Q. Li, H.L. Wang, L.Y. Zi, J.J. Zhang, Y.S. Zhang, *Ceram. Int.* **41**, 10634–10643 (2015)
59. D. Y.Lin, J. Li, G. Xiao Hu, J. Wang, W. Li, X. Fu, *J. Phys. Chem.* **116**, 5764–5772 (2012)
60. R. Wang, X. Wang, X. Xi, R. Hu, G. Jiang, *Adv. Mater. Sci. Eng.* (2012). <https://doi.org/10.1155/2012/409379>